Check for updates

Surface functionalized chalcogenides for highly selective removal of Hg²⁺†

Hao-Chen Jie,[ab] Zhi-Qing Lan,[ab] Ke-Feng Li,[bc] Xiao-Liang Ye,*[b] Shui-Lin Duan,[ab] Zhi-Hua Fu,*[b] Guan-E Wang (iD) *[b] and Gang Xu (iD) [b]

In this study, a crystalline material CuPMTT was synthesized *via* coordination self-assembly strategy. The surfaces of CuPMTT are densely populated with thiol groups that effectively capture Hg²⁺ ions, achieving an adsorption rate nearing 90% and a separation coefficient of 4.51 against Cu²⁺, thus outperforming conventional adsorbents and presenting a significant advancement in environmental protection chemistry.

Mercury ions (Hg²⁺) are potent environmental toxins with severe implications for human health, capable of causing neurological damage, renal impairment, and developmental issues.[1–7] Their propensity for bioaccumulation and biomagnification along the food chain necessitates the critical importance of Hg²⁺ removal from the environment.[8] The development of effective remediation strategies, such as the synthesis of advanced adsorbent materials, is imperative to mitigate the pervasive impacts of Hg ions on ecosystems and to safeguard public health, underscoring the urgency of environmental cleanup efforts.[9]

In the quest to remediate mercury (Hg²⁺) contamination, a plethora of techniques has emerged, encompassing electrodeposition, membrane separation, chemical precipitation, ion exchange, and adsorption.[10–17] Among these, adsorption has garnered significant interest owing to its merits of cost-effectiveness, high efficiency, minimal environmental impact, and straightforward implementation.[18,19] The crux of the adsorption process

hinges on the engineering of adsorbent materials.[20] Traditional adsorbents, such as clay minerals, zeolites, and porous silicon, are frequently utilized. Nonetheless, these materials are not without their limitations, including suboptimal selectivity and limited adsorption capacity.[19] Consequently, the development of adsorbent materials that can offer both high adsorption capacity and selectivity for Hg²⁺ remains a formidable challenge in the field of environmental chemistry.[21]

Coordination polymers (CPs) stand out as superior materials for ion adsorption, leveraging their customizable ion adsorption sites.[22,23] Given that Hg²⁺ is characterized as a soft acid and thiol groups are recognized as soft bases, the principles of the Soft Hard Acid Base (HSAB) theory dictate that soft bases exhibit a higher affinity for soft acids.[24] Consequently, this makes compounds featuring uncoordinated thiol groups particularly effective as Hg²⁺ adsorbents.[25] However, the potent chelating nature of thiol groups can lead to the saturation of all available thiol coordination sites upon interaction with metal ions, potentially causing material deactivation. Thus, the challenge lies in the strategic design of coordination polymers that incorporate thiol active sites in a manner that prevents over coordination, ensuring the sustained performance of the adsorbent material.[26]

The intricate coordination chemistry of ligands is significantly shaped by the chemical environment of the surrounding atoms, which dynamically tune the coordination capabilities of ligand across different sites.[27] Organic molecules possessing resonant structures are characterized by a dynamic equilibrium, which allows for the generation of unique coordination spheres. Capitalizing on this principle, this study employs pyrimidine 2,4,6(1H,3H,5H)-trithione (PMTT), an organic ligand with an asymmetric architecture, to complex with Cu⁺ ions, yielding the coordination polymer CuPMTT.[28] The crystallographic analysis, facilitated by three-dimensional rotational electron diffraction (3D ED), reveals that CuPMTT adopts a two-dimensional layered structure,

[a] College of Chemistry, Fuzhou University, Fuzhou City, Fujian Province 350108, P. R. China

[b] State Key Laboratory of Structural Chemistry and Fujian Institute of Research on the Structure of Matter, Chinese Academy of Sciences, Fuzhou 350002, P. R. China. E-mail: yexl@fjirsm.ac.cn, zhihuafu@outlook.com, gewang@fjirsm.ac.cn

[c] College of Chemistry and Materials Science, Fujian Normal University, 32 Shangsan Road, Fuzhou 350007, P. R. China.

replete with uncoordinated thione groups that dangle from the upper and lower layer of CuPMTT. These pendant thiol groups endow CuPMTT with superior adsorptive capacity and selectivity for Hg^{2+} ions, achieving an adsorption efficiency nearing 90%, which surpasses the performance of most conventional adsorbents documented to date. Kinetic examinations of the adsorption dynamics demonstrate that CuPMTT can rapidly sequester Hg^{2+} within seconds at ambient conditions. Collectively, the remarkable Hg^{2+} sequestration capabilities of CuPMTT underscore its significant potential as a research avenue for environmental conservation efforts.

PMTT as an organic ligand featuring an asymmetric structure, exists in two tautomeric forms (Fig. 1a). The XPS test results reveal that in PMTT, nitrogen (N) exists in both N–H (399.93 eV) and C=N (398.62 eV) peaks (Fig. S1†), confirming the presence of tautomeric forms in PMTT. Upon tautomerization, two thione moieties convert (C=S) into thiol groups (–SH), which are more inclined to coordinate with Cu. This strategic coordination leaves another thione group as an active site for the selective adsorption of Hg^{2+} ions. Employing a solvothermal synthesis approach, we successfully cultivated CuPMTT microcrystal. However, the crystal dimensions, measuring less than 20 μm as observed under an optical microscope (Fig. S2†), presented a challenge for structural characterization via standard single-crystal X-ray diffraction (SCXRD) techniques.[29] To circumvent this, we adopted three-dimensional electron diffraction (3D ED), which was proved to solve the structural analysis from a micro-sized crystal, to elucidate the crystal structure of the CuPMTT microcrystal.[30] The 3D ED data were recorded on a JEOL JEM2100 microscope (200 kV) using an ultra high-speed hybrid pixel detector. Instamatic was used for 3D ED data collection, with every 10th frame being used to generate an

image to trace the crystal.[31] The goniometer rotation speed was set at 0.45° s^{-1}, and the exposure time was set at 0.5 s per frame. The total tilting angle range is 133.78°. The reconstructed 3D reciprocal lattices of CuPMTT were depicted in Fig. 1b. The monoclinic unit cell parameters (a = 11.55, b = 10.71, c = 27.24 Å, α = 90, β = 97.80, and γ = 90°) could be deduced from this data set, and the possible space groups ($P_{2(1)}$ and P_c) could be obtained based on the reflection conditions as demonstrated in Fig. 1c. The 3D ED data were processed with XDS package.[32] The dataset has a signal-to-noise ratio of 4.58 within the resolution of 1.69 Å. Due to the limitation of the goniometer tilting range, the data completeness is 0.774. Its initial structural model was solved by the direct method implemented in Shelxt with the space group of P_c.

As delineated in Fig. 1d, each copper atom is ensconced within a tetrahedral coordination environment, ligated by four sulfur atoms derived from four distinct ligands, thus constituting a [CuS$_4$] motif, with the copper atom positioned at the geometric center of the tetrahedron. The sulfur atoms engaged in the coordination with the copper originate from the thiol groups (–SH) present in two different isomers. These [CuS$_4$] tetrahedra coalesce into dimers by corner-sharing of sulfur atoms, and these dimers are interlinked via the terminal ends of the ligands, culminating in a two-dimensional, layered architecture. Notably, the functional groups that remain uncoordinated are situated on the periphery of the structure. The X-ray photoelectron spectroscopy (XPS) analysis of the S element in CuPMTT, as depicted in Fig. S3,† reveals the presence of –SH and C=S functional groups, with respective atomic percentages of 9.5% and 9.6%. These two-dimensional layers are further integrated into a three-dimensional framework through van der Waals forces, establishing a robust and intricate network. This structural arrangement may be pivotal for the exceptional adsorptive properties, particularly its affinity and selectivity for Hg^{2+} ions.

The phase purity and crystallinity of the CuPMTT were authenticated through powder X-ray diffraction (PXRD) analysis, as depicted in Fig. 2a. The PXRD diffraction
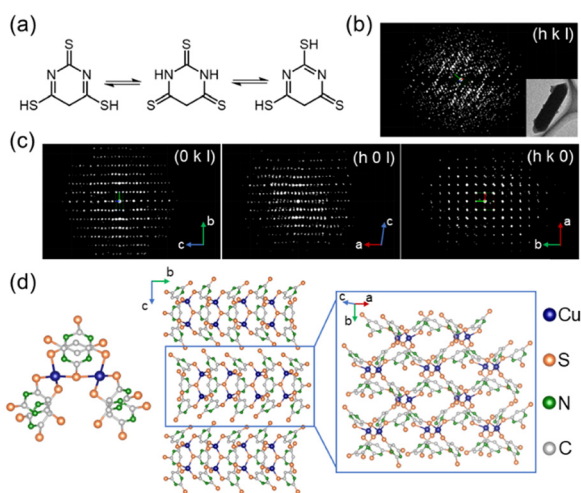

Fig. 1 (a) Schematic diagram of isomorphic transformation in PMTT. (b) The reconstructed 3D reciprocal space of CuPMTT. (c) Three 2D slices (0kl), (h0l), (hk0) cut from the 3D reciprocal lattice. The unit cell axes a*, b* and c* are shown in red, green and blue, respectively. (d) Schematic diagram of CuPMTT structure.
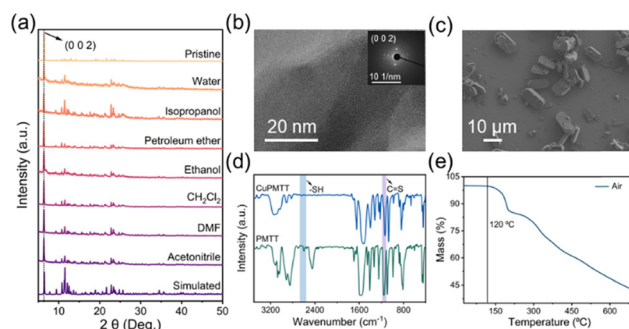

Fig. 2 Basic characterization of CuPMTT crystal material: (a) PXRD patterns after immersion in different solvents. (b) TEM image of CuPMTT$_{(0\ 0\ 2)}$. (c) SEM image of CuPMTT crystal. (d) Infrared spectra of CuPMTT and PMTT. (e) TG curve in air.

patterns suggest that CuPMTT crystals predominantly exhibit growth along the (0 0 2) lattice plane, resulting in a surface rich in thiol sites. This observation was further substantiated by transmission electron microscopy (TEM) examination, as illustrated in Fig. 2b. Scanning electron microscopy (SEM) was utilized to characterize the morphology of the CuPMTT, which are observed to be sheet-like and aggregate into hexagonal columns, with uniform dimensions of approximately 10 μm in both length and width, as shown in Fig. 2c. Infrared (IR) spectroscopy was conducted to analyse the CuPMTT and the ligand separately (Fig. 2d). PMTT and CuPMTT both exhibit infrared absorption peaks corresponding to the C=S bond (1140 cm^{-1}). It is noteworthy that the IR spectrum of the ligand also exhibits a peak for thiol group at 2630 cm^{-1}, indicating the presence of tautomerism in PMTT, which is prior to coordination with Cu$^+$ ions. A distinct thiol peak at 2630 cm^{-1} was detected in the compound, confirming the abundance of –SH active sites on the surface of CuPMTT. CuPMTT demonstrated excellent chemical and thermal stability. After immersing the sample in various solvents for an extended period, the PXRD patterns remained consistent with the simulated patterns, signifying the robust environmental stability. The thermogravimetric analysis, as seen in Fig. 2e, indicates that the material is stable up to 120 °C. Such stability is a prerequisite for the practical application of CuPMTT, providing a reliable foundation for its potential use in environmental remediation and other relevant fields.

To ascertain the adsorptive capacity and selectivity of CuPMTT for a spectrum of metal ions, an in-depth analysis was conducted on its affinity for various alkaline earth and transition metal ions of physiological and environmental significance, including Cu^{2+}, Na$^+$, K$^+$, Zn^{2+}, Mg^{2+}, Cd^{2+}, Co^{3+}, Fe^{2+}, Fe^{3+}, Ni^{2+}, Sr^{2+}, Mn^{2+} and Hg^{2+}. Utilizing inductively coupled plasma optical emission spectrometry (ICP-OES), it was that CuPMTT exhibits negligible adsorption for other ions, while it displays a pronounced selective adsorption for Hg^{2+} ions, as depicted in Fig. 3a. Furthermore, the presence

of various anions exerts no significant influence on the Hg^{2+} adsorption of CuPMTT (Fig. S4†). The adsorption rate of CuPMTT towards Hg^{2+} is nearing 90%. The XRD analysis was conducted on the CuPMTT post-adsorption (Fig. S5†). The results reveal a significant alteration in the XRD pattern of the material after the adsorption process, suggesting the irreversibility of the adsorption. The adsorption selectivity coefficient data (Table S1†) reveals the separation coefficient stands at 4.51 in relation to the adsorption of the most interfering Cu^{2+} ions, highlighting the remarkable selectivity of CuPMTT for Hg^{2+} ions.

The UV-vis spectrophotometer was employed to monitor the absorbance changes of CuPMTT dispersion during post-adsorption of Hg^{2+} at varying concentrations (Fig. 3b and S6†). CuPMTT is characterized by two principal absorption peaks at approximately 280 nm and 370 nm (Fig. S7†). With an increase in Hg^{2+} concentration, there is a corresponding decrease in the absorbance peak of the sample (Fig. 3b and c), where a higher concentration of mercury ions correlates with a more significant reduction in the absorbance peak. The detection limit of CuPMTT is 7.36 mmol (Fig. S8†). Additionally, as the pH of the solution decreases, there is a corresponding reduction in the absorbance intensity of CuPMTT (Fig. S9†). This suggests that the adsorption performance is enhanced under acidic conditions relative to alkaline conditions. This improvement in adsorption is likely due to the increased concentration of free hydrogen ions in the solution under acidic conditions, which promotes the conversion of C=S to –SH groups, thereby augmenting the adsorptive capacity of CuPMTT for Hg^{2+} ions. The kinetic studies focusing on the reduction of the UV absorbance peak at 370 nm confirm that an elevated Hg^{2+} concentration leads to a more pronounced decrease in the absorbance peak of CuPMTT (Fig. 3d and S10†). By dynamically modeling the relationship between absorbance intensity and time (Fig. 3e), it is evident that the adsorption rate increases with the concentration of Hg^{2+}. The ion absorption rate constant can reach to 1.8 mmol s^{-1} at a
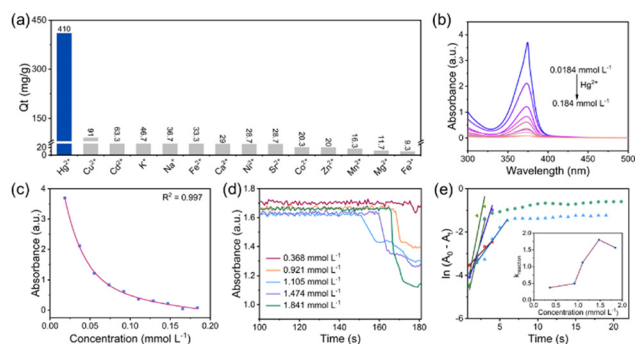

Fig. 3 (a) Selective adsorption of Hg^{2+} by CuPMTT. (b) The UV absorption of CuPMTT after adsorption of different concentrations of Hg^{2+}. (c) The relationship between the adsorption of CuPMTT and the concentrations of Hg^{2+}. (d) The kinetic curve of CuPMTT adsorption of Hg^{2+}. (e) Curve fitting of the absorption rate constant.
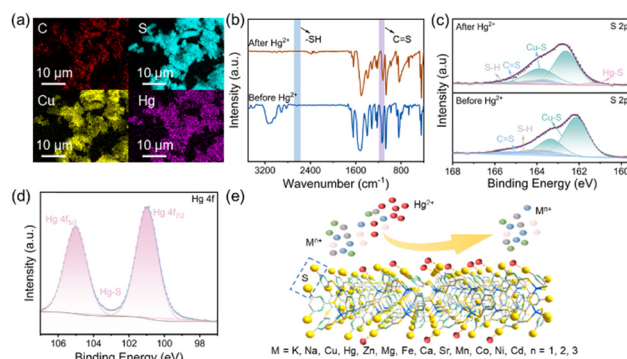

Fig. 4 (a) EDS spectrum of the adsorbed compound. (b) Infrared spectra of CuPMTT before and after adsorption. (c) XPS spectra of S element before and after adsorption. (d) XPS spectrum of Hg element after adsorption. (e) Schematic diagram of CuPMTT adsorption mechanism.

concentration of 1.474 mmol L^{-1}, indicative CuPMTT can swiftly encapsulate Hg^{2+} ions within a few seconds.

The energy dispersive spectrometer (EDS) image post-adsorption, as presented in Fig. 4a, reveals a uniform distribution of the Hg element across the compound, which is a clear indication of the adsorptive affinity for mercury. This homogeneous distribution suggests that the adsorption process is effective and widespread across the surface of CuPMTT. Furthermore, the infrared spectroscopic (IR) analysis of CuPMTT both prior to and following the adsorption of Hg^{2+}, as depicted in Fig. 4b, provides further insights into the adsorption mechanism. Before the adsorption process, the IR spectrum exhibits a distinct thiol absorption peak at a wavelength of 2630 cm^{-1}, which is characteristic of the –SH groups present on the surface of the material. However, upon completion of the Hg^{2+} adsorption, this thiol peak vanishes. This disappearance implies that the Hg^{2+} ions likely form strong coordination bonds with the thiol groups on the surface of the CuPMTT. The formation of these Hg–S bonds results in the consumption of the available thiol groups, thereby causing the characteristic thiol peak to disappear from the IR spectrum. It is worth mentioning that the infrared absorption peak of C=S at 1140 cm^{-1} exhibits a notable reduction following the adsorption of CuPMTT. This phenomenon suggests that during the adsorption process, some C=S entities coordinate with Hg^{2+} in the solution, leading to a weakening of the peak intensity.

XPS was employed to investigate and analyze the elemental and chemical states of CuPMTT both before and after the adsorption of Hg^{2+}. The analysis results revealed that prior to Hg^{2+} adsorption, there was an absence of an Hg spectral peak (Fig. S11†), which is expected as the material does not initially contain mercury. Upon the adsorption of Hg^{2+}, a distinct Hg spectral peak emerges, confirming the successful uptake of Hg^{2+} by CuPMTT. A significant transformation was also observed in the XPS spectrum corresponding to the sulfur (S) element. The binding energy of S in CuPMTT primarily attributed to Cu–S, C=S, and –SH groups. After the adsorption process was concluded, a distinct set of S 2p spin–orbit splitting peaks emerged of sulfur at 161.38 eV and 162.56 eV, alongside the previously mentioned three peaks. Subsequent analysis revealed that these peaks corresponded to the characteristic binding energy of HgS.[33] Upon comparison with pre-adsorption spectra, it was noted that the peaks corresponding to –SH and C=S functionalities exhibited a decrease, with –SH showing a more pronounced decrease. This suggests the involvement of both groups in the coordination process with Hg^{2+}. Integration with infrared data further revealed a higher affinity of –SH over C=S in the coordination with Hg^{2+}.

Furthermore, in the XPS spectrum subsequent to Hg^{2+} (Fig. 4d), two pronounced binding energy appeared at 104.98 eV and 100.88 eV, which are assigned to the Hg 4f 5/2 and Hg 4f 7/2 levels, respectively. The energy difference of 4.1 eV between these two peaks is characteristic of the spin–orbit splitting of Hg 4f levels, further confirming the presence of Hg in the material. Drawing upon the aforementioned analysis, the adsorption mechanism of CuPMTT may be due to the abundance of thiocarbonyl and thiol active sites on the surface of the CuPMTT material. Mercury ions bind to the thiocarbonyl and thiol groups on the material's surface, leading to the substantial adsorption of Hg ions by the dispersed CuPMTT in the solution (Fig. 4e). This process achieves the removal of mercury.

Conclusions

In conclusion, this work employs a facile solvothermal technique to meticulously engineer CuPMTT crystalline materials, subsequently subjected to a structural interrogation *via* the precision of three-dimensional rotational electron diffraction (3D ED). The resultant material is replete with uncoordinated thiol and thione groups that are elegantly suspended on the upper and lower strata of the layer. CuPMTT has been demonstrated to possess a marked selectivity for Hg^{2+} ions, evidenced by a separation coefficient of 4.51 in the context of Hg^{2+} and Cu^{2+}, and an impressive adsorption rate that hovers near 90% for Hg^{2+}. This performance not only eclipses the limitations of conventional Hg^{2+} adsorbents, which are frequently hampered by their modest adsorption capacities and selectivities, but also sets a new precedent in the realm of mercury capture. Furthermore, an intriguing correlation between the UV absorption peak and the concentration of Hg^{2+} has been unveiled in this study, indicating that CuPMTT is engaged in a rapid adsorption process, characterized by a rate constant that reaches an impressive 1.8 mmol s^{-1}. This enables the material to swiftly encapsulate Hg^{2+} ions, accomplishing the adsorption within a few seconds. Furthermore, our investigation into the adsorption mechanism of CuPMTT revealed that the thiol and thione groups exhibit a superior coordination affinity towards Hg^{2+}, highlighting their enhanced capability in the adsorption process. This work not only provides certain reference significance for designing coordination polymers, but also provides certain research value for environmental protection.

Data availability

The data that support the findings of this study are available from the corresponding author upon reasonable request.

Author contributions

H.-C. J., and G.-E. W. conceived the idea. H.-C. J., G.-E W., Z.-Q. L., K.-F. L., X.-L. Y., and S.-L. D. designed the experiments, collected and analyzed the data. X.-L. Y., Z.-H. F. and G. X. assisted with the experiments and characterizations. H.-C. J. and G.-E. W. wrote the manuscript. All authors discussed the results and commented on the manuscript.

Conflicts of interest

There are no conflicts to declare.

Acknowledgements

Notes and references

1 Y. Tao, X. H. Xiong, J. B. Xiong, L. X. Yang, Y. L. Fan, H. Feng and F. Luo, *J. Solid State Chem.*, 2020, **282**, 121126.

2 M. Bahrani-Pour, A. Beheshti, T. Sedaghat, E. Hoveizi, N. Naseri, P. Mayer and R. Centore, *Dalton Trans.*, 2023, **52**, 683–695.

3 P. Prema, V. Veeramanikandan, K. Rameshkumar, M. K. Gatasheh, A. A. Hatamleh, R. Balasubramani and P. Balaji, *Environ. Res.*, 2022, **204**, 111915.

4 J. Wang, T. Liu, B. Wang, Z. Li, Y. Niu, H. Chen and Y. Zhang, *Chin. Chem. Lett.*, 2024, **35**, 109900.

5 S. S. Ghasemi, M. Hadavifar, B. Maleki and E. Mohammadnia, *J. Water Process. Eng.*, 2019, **32**, 100965.

6 Q. Pan, Q. Hong, Y. Fan, X. Sun, W. Huang, N. Yan, Z. Qu and H. Xu, *Sep. Purif. Technol.*, 2024, **333**, 125917.

7 X. Zhao, J. Li, S. Mu, W. He, D. Zhang, X. Wu, C. Wang and H. Zeng, *Environ. Pollut.*, 2021, **268**, 115705.

8 D. Zhang, G. Crini, E. Lichtfouse, B. Rhimi and C. Wang, *Chem. Rec.*, 2020, **20**, 1220–1234.

9 R. Jesuraj and P. Perumal, *Anal. Methods*, 2024, **16**, 3562–3576.

10 Y. M. Zhao, L. Cheng, K. Y. Wang, X. Hao, J. Wang, J. Y. Zhu, M. Sun and C. Wang, *Adv. Funct. Mater.*, 2022, **32**, 2112717.

11 C. Bunditboondee, J. Lohwacharin, E. Khan, S. Kulyakoon and K. Laohhasurayotin, *J. Environ. Manage.*, 2021, **288**, 112443.

12 C. Wang, G. Lin, J. Zhao, S. Wang and L. Zhang, *Chem. Eng. J.*, 2020, **388**, 124221.

13 M. Wang, Y. Li, D. Zhao, L. Zhuang, G. Yang and Y. Gong, *Chem. Eng. J.*, 2020, **381**, 122664.

14 B. Zeng, W. Wang, S. He, G. Lin, W. Du, J. Chang and Z. Ding, *Nano Mater. Sci.*, 2021, **3**, 429–439.

15 B. Wang, K. Wu, T. Liu, Z. Cheng, Y. Liu, Y. Liu and Y. Niu, *J. Hazard. Mater.*, 2023, **442**, 130121.

16 L. Luan, B. Tang, Y. Liu, A. Wang, B. Zhang, W. Xu and Y. Niu, *Sep. Purif. Technol.*, 2021, **257**, 117902.

17 L. Lang, B. Wang, T. Liu, J. Wang, L. Zhu, Y. Liu and Y. Niu, *Chem. Eng. J.*, 2023, **477**, 147310.

18 K.-Y. Wang, M.-Y. Li, L. Cheng, X. Hao and C. Wang, *Inorg. Chem. Front.*, 2024, **11**, 3229–3244.

19 B. Zeng, J. Li, C. Xiong, G. Lin, W. Wang and Z. Wu, *J. Cleaner Prod.*, 2022, **337**, 130551.

20 J. Li, G. Lin, F. Tan, L. Fu, B. Zeng, S. Wang, T. Hu and L. Zhang, *J. Colloid Interface Sci.*, 2023, **651**, 659–668.

21 Y.-M. Zhao, M. Sun, L. Cheng, K.-Y. Wang, Y. Liu, J.-Y. Zhu, S. Zhang and C. Wang, *J. Hazard. Mater.*, 2022, **425**, 128007.

22 J. Zhang, L. Chen, X. Dai, L. Zhu, C. Xiao, L. Xu, Z. Zhang, E. V. Alekseev, Y. Wang, C. Zhang, H. Zhang, Y. Wang, J. Diwu, Z. Chai and S. Wang, *Chem*, 2019, **5**, 977–994.

23 M. Lippi and M. Cametti, *Coord. Chem. Rev.*, 2021, **430**, 213661.

24 S. Ali, Z. Zuhra, S. Ali, Q. Han, M. Ahmad and Z. Wang, *Chemosphere*, 2021, **284**, 131305.

25 R. Sun, G. Luo, M. Yu, L. Wang, X. Lu, X. Li and H. Yao, *Chem. Eng. J.*, 2023, **477**, 147061.

26 A. Ostasz and A. M. Kirillov, *Polymer*, 2020, **12**, 1329.

27 J. Yang, S. Xie, H. Zhang, W. Xu, A. Dong and Y. Tang, *Chem. Commun.*, 2022, **58**, 6849–6852.

28 G.-N. Liu, X.-N. Tang, J.-S. Guo, Q.-S. Liu, C. Ye, C. Li, G. Xu and G.-E. Wang, *Sens. Actuators, B*, 2024, **399**, 134864.

29 C. Nie, N. Yan, C. Liao, C. Ma, X. Liu, J. Wang, G. Li, P. Guo and Z. Liu, *J. Am. Chem. Soc.*, 2024, **146**, 10257–10262.

30 I. Andrusenko, V. Hamilton, E. Mugnaioli, A. Lanza, C. Hall, J. Potticary, S. R. Hall and M. Gemmi, *Angew. Chem., Int. Ed.*, 2019, **58**, 10919–10922.

31 M. O. Cichocka, J. Ångström, B. Wang, X. Zou and S. Smeets, *J. Appl. Crystallogr.*, 2018, **51**, 1652–1661.

32 W. Kabsch, *Acta Crystallogr., Sect. D: Biol. Crystallogr.*, 2010, **66**, 133–144.

33 X. Zhang, X. Xing, L. Cui, P. Sun, J. Tang, J. Chen and Y. Dong, *Fuel*, 2023, **332**, 125926.